Monthly Notices
of the
ROYAL ASTRONOMICAL SOCIETY

Mon. Not. R. Astron. Soc. **415,** 3473–3484 (2011) doi:10.1111/j.1365-2966.2011.18959.x

Physical conditions of the interstellar medium of high-redshift, strongly lensed submillimetre galaxies from the *Herschel*-ATLAS⋆

I. Valtchanov,[1]† J. Virdee,[2,3] R. J. Ivison,[4,5] B. Swinyard,[2,6] P. van der Werf,[5,7] D. Rigopoulou,[2,3] E. da Cunha,[8,9] R. Lupu,[10] D. J. Benford,[11] D. Riechers,[12] Ian Smail,[13] M. Jarvis,[14] C. Pearson,[2] H. Gomez,[15] R. Hopwood,[16] B. Altieri,[1] M. Birkinshaw,[17] D. Coia,[1] L. Conversi,[1] A. Cooray,[18] G. De Zotti,[19,20] L. Dunne,[21] D. Frayer,[22] L. Leeuw,[23,24] A. Marston,[1] M. Negrello,[25] M. Sanchez Portal,[1] D. Scott,[26] M. A. Thompson,[21] M. Vaccari,[27] M. Baes,[28] D. Clements,[16] M. J. Michałowski,[5] H. Dannerbauer,[29] S. Serjeant,[25] R. Auld,[15] S. Buttiglione,[27] A. Cava,[30] A. Dariush,[15,31] S. Dye,[15] S. Eales,[15] J. Fritz,[28] E. Ibar,[4] S. Maddox,[21] E. Pascale,[15] M. Pohlen,[15] E. Rigby,[21] G. Rodighiero,[27] D. J. B. Smith,[21] P. Temi,[32] J. Carpenter,[12] A. Bolatto,[33] M. Gurwell[34] and J. D. Vieira[12]‡

[1]*European Space Astronomy Centre, Herschel Science Centre, ESA, 28691 Villanueva de la Cañada, Spain*
[2]*RAL Space, STFC-Rutherford Appleton Laboratory, Harwell Campus, Chilton, Didcot, Oxon OX11 0QX*
[3]*Oxford Astrophysics, Denys Wilkinson Building, University of Oxford, Keble Road, Oxford OX1 3RH*
[4]*UK Astronomy Technology Centre, Royal Observatory, Blackford Hill, Edinburgh EH9 3HJ*
[5]*SUPA, Institute for Astronomy, University of Edinburgh, Blackford Hill, Edinburgh EH9 3HJ*
[6]*Department of Physics and Astronomy, University College London, Gower Street, London WC1E 6BT*
[7]*Leiden Observatory, Leiden University, PO Box 9513, 2300 RA Leiden, the Netherlands*
[8]*Department of Physics, University of Crete, 71003 Heraklion, Greece*
[9]*Max-Planck-Institut fur Astronomie, Konigstuhl 17, 69117 Heidelberg, Germany*
[10]*Department of Physics and Astronomy, University of Pennsylvania, Philadelphia, PA 19104, USA*
[11]*Observational Cosmology Laboratory (Code 665), NASA Goddard Space Flight Center, Greenbelt, MD 20771, USA*
[12]*California Institute of Technology, 1200 E. California Blvd., MC 249-17, Pasadena, CA 91125, USA*
[13]*Department of Physics, Institute for Computational Cosmology, Durham University, Durham DH1 3LE*
[14]*Centre for Astrophysics Research, Science and Technology Research Centre, University of Hertfordshire, Herts AL10 9AB*
[15]*School of Physics and Astronomy, Cardiff University, The Parade, Cardiff CF24 3AA*
[16]*Astrophysics Group, Imperial College, Blackett Laboratory, Prince Consort Road, London SW7 2AZ*
[17]*HH Wills Physics Laboratory, University of Bristol, Tyndall Avenue, Bristol BS8 1TL*
[18]*Department of Physics & Astronomy, University of California, Irvine, CA 92697, USA*
[19]*INAF, Osservatorio Astronomico di Padova, Vicolo Osservatorio 5, I-35122 Padova, Italy*
[20]*Scuola Internazionale Superiore de Studi Avanzati, Via Bonomea 265, I-34136 Trieste, Italy*
[21]*School of Physics and Astronomy, University of Nottingham, University Park, Nottingham NG7 2RD*
[22]*National Radio Astronomy Observatory, PO Box 2, Green Bank, WV 24944, USA*
[23]*Physics Department, University of Johannesburg, PO Box 524, Auckland Park 2006, South Africa*
[24]*SETI Institute, 515 N. Whishman Avenue, Mountain View, CA 94043, USA*
[25]*Department of Physics & Astronomy, The Open University, Milton Keynes MK7 6AA*
[26]*Department of Physics & Astronomy, University of British Columbia, 6224 Agricultural Road, Vancouver, BC V6T 1Z1, Canada*
[27]*Dipartimento di Astronomia, Università di Padova, vicolo Osservatorio 3, I-35122 Padova, Italy*
[28]*Sterrenkundig Observatorium, Universiteit Gent, Krijgslaan 281 S9, B-9000 Gent, Belgium*
[29]*DAPNIA/Service d'Astrophysique, CEA Saclay, Orme des Merisiers, 91191 Gif-sur-Yvette, France*
[30]*Departamento de Astrofísica, Facultad de CC. Físicas, Universidad Complutense de Madrid, E-28040 Madrid, Spain*
[31]*School of Astronomy, Institute for Research in Fundamental Sciences (IPM), PO Box 19395-5746, Tehran, Iran*
[32]*Astrophysics Branch, NASA Ames Research Center, Mail Stop 245-6, Moffet Field, CA 94035, USA*
[33]*Department of Astronomy, University of Maryland, College Park, MD 20742, USA*
[34]*Harvard–Smithsonian Center for Astrophysics, Cambridge, MA 02138, USA*

Accepted 2011 April 24. Received 2011 April 20; in original form 2011 March 21

⋆*Herschel* is an ESA space observatory with science instruments provided by European-led Principal Investigator consortia and with important participation from NASA.

†E-mail: ivaltchanov@sciops.esa.int

‡Correction added after online publication 2011 July 12: author added.

© 2011 The Authors

Downloaded from https://academic.oup.com/mnras/article/415/3473/1748743
by Imperial College London Library user
on 11 December 2017

ABSTRACT

We present *Herschel*-Spectral and Photometric Imaging Receiver (SPIRE) Fourier transform spectrometer (FTS) and radio follow-up observations of two *Herschel*-Astrophysical Terahertz Large Area Survey (H-ATLAS)-detected strongly lensed distant galaxies. In one of the targeted galaxies H-ATLAS J090311.6+003906 (SDP.81), we detect [O III] 88 μm and [C II] 158 μm lines at a signal-to-noise ratio of ∼5. We do not have any positive line identification in the other fainter target H-ATLAS J091305.0−005343 (SDP.130). Currently, SDP.81 is the faintest submillimetre galaxy with positive line detections with the FTS, with continuum flux just below 200 mJy in the 200–600 μm wavelength range. The derived redshift of SDP.81 from the two detections is $z = 3.043 \pm 0.012$, in agreement with ground-based CO measurements. This is the first detection by *Herschel* of the [O III] 88 μm line in a galaxy at redshift higher than 0.05. Comparing the observed lines and line ratios with a grid of photodissociation region (PDR) models with different physical conditions, we derive the PDR cloud density $n \approx 2000\,\mathrm{cm}^{-3}$ and the far-ultraviolet ionizing radiation field $G_0 \approx 200$ (in units of the Habing field – the local Galactic interstellar radiation field of 1.6×10^{-6} W m^{-2}). Using the CO-derived molecular mass and the PDR properties, we estimate the effective radius of the emitting region to be 500–700 pc. These characteristics are typical for star-forming, high-redshift galaxies. The radio observations indicate that SDP.81 deviates significantly from the local far-infrared/radio (FIR/radio) correlation, which hints that some fraction of the radio emission is coming from an active galactic nucleus (AGN). The constraints on the source size from millimetre-wave observations put a very conservative upper limit of the possible AGN contribution to less than 33 per cent. These indications, together with the high [O III]/FIR ratio and the upper limit of [O I] 63 μm/[C II] 158 μm, suggest that some fraction of the ionizing radiation is likely to originate from the AGN.

Key words: galaxies: evolution – galaxies: individual: SDP.81: H-ATLAS J090311.6+003906 – galaxies: individual: SDP.130: H-ATLAS J091305.0−005343 – infrared: galaxies – radio continuum: galaxies – submillimetre: ISM.

1 INTRODUCTION

The detection of large numbers of high-redshift, optically obscured, massive star-forming galaxies by ground-based submillimetre instruments such as Submillimetre Common-User Bolometer Array and Max Planck Millimetre Bolometer (MAMBO) was a surprise and a major discovery (e.g. Smail, Ivison & Blain 1997). These submillimetre galaxies (SMGs) present amongst the most difficult obstacles for models of galaxy formation and evolution (e.g. Baugh et al. 2005). The SMGs are a subset of the dusty star-forming galaxies that account for more than half of the far-infrared (FIR) background (Devlin et al. 2009). Their star formation rates are orders of magnitudes higher than most galaxies in the local Universe, and they are considered the precursors of today's most massive elliptical or bulge galaxies (Lilly et al. 1999; Swinbank et al. 2006).

Due to the fact that more than half of the light from the SMGs is absorbed and reprocessed by dust, it is exceedingly important to study these sources at their peak emission, which occurs in the FIR. Prior to the *Herschel* (Pilbratt et al. 2010), ground-based and balloon-borne studies of SMGs were limited to small fields and produced modest samples detected at low significance. This situation is changing dramatically with the number of wide-field surveys with *Herschel Space Observatory*, such as the *Herschel*-Astrophysical Terahertz Large Area Survey (H-ATLAS). H-ATLAS is the largest *Herschel* Open Time Key Programme (Eales et al. 2010), and will map 550 deg^2 in six extragalactic fields in five photometric bands, using in parallel mode both the Photodetector Array Camera & Spectrometer (PACS; Poglitsch et al. 2010) and the SPIRE (Griffin et al. 2010) instruments. One of the most interesting results of H-ATLAS will be the detection of a significant number of gravitationally lensed objects in the distant ($z > 2$) Universe. This is possible in such a shallow but large area survey because of the combined effects of a strong negative *K*-correction and steep number counts in the SPIRE 500-μm waveband (e.g. Blain 1996). Objects brighter than 100 mJy at 500 μm will be a mixture of lensed high-redshift galaxies, nearby galaxies and flat-spectrum radio sources (De Zotti et al. 2005; Negrello et al. 2007; Eales et al. 2010) and current models predict that H-ATLAS will detect some ∼350 strongly lensed objects at 500 μm at redshifts >1 (Negrello et al. 2007).

High-redshift, bright SMGs open a new possibility for the detailed study of the physical conditions of the interstellar medium (ISM), at rest-frame FIR. Atomic emission lines in this range provide the major coolants for neutral gas exposed to the far-ultraviolet (FUV) ionizing flux of nearby early-type stars. Star-forming molecular clouds where the physical processes are dominated by FUV photons are called photodissociation regions (PDRs; e.g. Hollenbach & Tielens 1997). FIR lines are not strongly affected by extinction in these regions, and so provide an excellent probe of the embedded stellar radiation fields and their effects on the physical conditions of the neutral gas. The majority of their cooling occurs via atomic fine-structure lines of [C II], [O I], [O III] (Brauher et al. 2008) and the molecular rotational ^{12}CO lines (Kramer et al. 2004). There have been several pre-*Herschel* efforts to study fine-structure lines for nearby as well as higher redshift galaxies, such as Stacey et al. (1991, 2010), Malhotra et al. (2001), Maiolino et al. (2005, 2009), Brauher et al. (2008), Walter et al. (2009a,b), Wagg et al. (2010), Ferkinhoff et al. (2010), Vasta et al. (2010) and

Downloaded from https://academic.oup.com/mnras/article-abstract/415/4/3473/1748743
by Imperial College London Library user
on 11 December 2017

Table 1. Positions and photometry measurements of SDP.81 and SDP.130. The quoted positions are those determined using IRAM PdBI at 0.62×0.30 arcsec^2 beam resolution (Neri et al. in preparation), thus accurate to <1 arcsec. The redshifts and the SPIRE photometry are taken from Negrello et al. (2010), while the PACS 160 μm measurements are from this work. The upper limits at 70 μm are 1σ.

Target ID	Redshift	RA (J2000)	Dec. (J2000)	S_{70} (mJy)	S_{160} (mJy)	S_{250} (mJy)	S_{350} (mJy)	S_{500} (mJy)
SDP.81	3.042 ± 0.001	09:03:11.6	+00:39:06.7	<8	51.4 ± 5.0	129.0 ± 6.6	181.9 ± 7.3	165.9 ± 9.3
SDP.130	2.625 ± 0.001	09:13:05.3	−00:53:42.8	<9	45.3 ± 7.7	105.0 ± 6.5	127.6 ± 7.2	107.5 ± 9.0

Hailey-Dunsheath et al. (2010), as well as molecular (CO) studies of SMGs, e.g. Greve et al. (2005), Tacconi et al. (2006, 2008), Daddi et al. (2009a,b), Riechers et al. (2010) and Danielson et al. (2011). *Herschel*, however, opens up a new frontier with its highly sensitive spectrometers, especially for observations of lines like [C II] at 158 μm at redshifts up to ∼3.

During *Herschel*'s Science Demonstration Phase, one of the H-ATLAS fields, GAMA9, was observed, covering $\sim 4 \times 4\,\mathrm{deg}^2$ (see Rigby et al. 2011 and Smith et al. 2011 for the H-ATLAS data in this field). The processing of the *Herschel* observations is presented in Ibar et al. (2010b) for the PACS and in Pascale et al. (2011) for the SPIRE observations. We have identified 11 sources with flux density at 500 μm $S_{500} \geq 100$ mJy, and the results of the analysis of these candidate lensed sources, from follow-up observations using facilities both on the ground and in space, are presented in Negrello et al. (2010), Lupu et al. (2010), Frayer et al. (2011) and Hopwood et al. (2011).

The subject of this paper is to present the SPIRE Fourier transform spectrometer (FTS) and radio observations and report on the first results from the FIR spectroscopy for two targets from Negrello et al. (2010): H-ATLAS J090311.6+003906 designated SDP.81 and H-ATLAS J091305.0−005343 designated SDP.130. Their positions, measured redshift and photometric properties in the FIR are shown in Table 1. Each of these two targets was initially associated with an elliptical galaxy, yet based on their spectral energy distribution (SED), peaking at ∼350 μm, it was clear that the foreground galaxy acts as a lens for a background source. Subsequent follow-up using Caltech Submillimeter Observatory/Z-Spec and Green Bank Telescope/Zpectrometer instruments detected several CO lines at a high signal-to-noise ratio (SNR) and secured a spectroscopic redshift of 3.042 ± 0.001 for SDP.81 and 2.625 ± 0.001 for SDP.130 (see Lupu et al. 2010; Negrello et al. 2010; Frayer et al. 2011 for more details).

The feasibility of the proposed FTS follow-up was well demonstrated during SPIRE's performance and verification phase. One bright, lensed, high-redshift SMG, SMM J2135−0102 at $z = 2.3$ (Swinbank et al. 2010), was observed with the SPIRE FTS, achieving a detection of the [C II] 158 μm line at 4.3σ [line flux of $(1.7 \pm 0.4) \times 10^{-17}$ W m^{-2}] as well as tentative detections of [O I] at 145.5 μm and [N II] at 122.1 μm (Ivison et al. 2010d).

The structure of the paper is as follows: in Section 2 we present the FTS and radio observations and the FTS-observing strategy. Some of the characteristics of the environment (telescope and instrument) during the FTS observations, relevant for the subsequent data processing, are also presented. The FTS data processing, with some details on the deviations from the standard *Herschel*-SPIRE FTS data processing, is described in Section 3. The results are presented in Section 4 and summarized in the conclusions (Section 5).

For all cosmological-dependent parameters we use $h = 0.73$, $\Omega_m = 0.24$ and flat geometry, i.e. $\Omega_\Lambda = 1 - \Omega_m = 0.76$ (Lahav & Liddle 2006). With these parameters the luminosity distances to redshifts 2.625 and 3.042 are 22.06 and 26.41 Gpc, respectively.

2 OBSERVATIONS

2.1 SPIRE FTS

The FTS observations were carried out on 2010 June 1 (*Herschel* observing day number 383). We targeted the two H-ATLAS-lensed candidates, SDP.81 and SDP.130, and a nearby (offset at ∼2′ arcmin) dark-sky region, devoid of sources and chosen using the available SPIRE maps. The three observations were done in a sequence: SDP.81 then the dark sky and then SDP.130, each one with exactly the same SPIRE-FTS observing template: 100 repetitions using single pointing mode, sparse spatial sampling and high spectral resolution. The total time for each observation, including overheads, was $3^{\mathrm{h}}52.^{\mathrm{m}}2$, with 66.6 s on-source time per FTS scan (one repetition consists of one forward and one reverse scan, i.e. two scans per repetition).

The measured absolute pointing error of *Herschel* is 2 arcsec (68 per cent; Pilbratt et al. 2010) – this is much smaller than the smallest FTS beam of ∼17 arcsec at 200 μm (Swinyard et al. 2010). The pointing stability of *Herschel* during the observation was excellent: during the 4 h of spectral scans the telescope jitter stayed within 0.14 arcsec (68 per cent) from the target position. The largest deviation was 0.54 arcsec.

The main source of emission in the FTS bands is the *Herschel* telescope itself, although this is a constant background as the telescope temperature does not change significantly on the time-scale of our observations. The emission of the telescope ranges from 100 to 1000 Jy in the FTS bands (Swinyard et al., in preparation). Targets such as SDP.81 and SDP.130, with continuum levels around or below 200 mJy are just a tiny fraction of this signal. That is why it is very important to have an off-source reference dark-sky measurement, performed as close in time as possible to the target observation, in order to be used to subtract the telescope and instrument contribution from the source spectrum (see Section 3).

By design, the FTS also has a second input port that sees a spectrometer calibration (SCAL) source, and this is the second source of significant thermal emission. Regardless of the fact that the SCAL source is not used and the lamp is turned off (see SPIRE OM 2010[1]), it stays at the instrument enclosure temperature and emits thermally in the two FTS bands. This instrument contribution is also removed with the help of the dark-sky observation. As SDP.130 is about 30 per cent fainter than SDP.81 at 350 μm and at a different redshift (see Table 1), we have added this observation as a second dark-sky measurement in order to decrease the noise of the reference subtraction for SDP.81.

During the observations the primary mirror temperature was on average 88.20 ± 0.06 K, the secondary mirror temperature stayed at 84.290 ± 0.004 K with variations at the mK level. The instrument

[1] The SPIRE Observers' Manual is available from the Herschel Science Centre: http://herschel.esac.esa.int/Docs/SPIRE/pdf/spire_om.pdf.

Downloaded from https://academic.oup.com/mnras/article-abstract/415/4/3473/1748743
by Imperial College London Library user
on 11 December 2017

enclosure temperature during the SDP.81 observation was 4.70–4.75 K, during the off-source dark-sky measurement it was 15 mK colder and 22 mK colder during the SDP.130 observation. Such seemingly small differences in the instrument and telescope temperatures, even at a level of a few mK, during the dark-sky and the target measurements, can lead to overall additive effect on the continuum level. Following Ivison et al. (2010d), we have used the three SPIRE photometry points at 250, 350 and 500 μm in order to recover the continuum level (see Section 3).

2.2 PACS photometry

In addition to the SPIRE FTS spectral scans, we did short PACS cross-linked mini-scan maps for each source at 70 and 160 μm (PACS blue and red bands). This was necessary because SDP.81 was not bright enough to be detected in the PACS parallel mode scans, while SDP.130 was not in the region covered by PACS in the PACS/SPIRE parallel mode. The PACS mini-scan maps were processed with version 5.0 of the *Herschel* Interactive Processing Environment (HIPE; Ott et al. 2010) using a standard data reduction script applying a temporal high-pass filter to remove the $1/f$ noise after masking the source for the filtering. The data cube was projected with the *photProject* task and the two scan directions were combined with the *Mosaic* task. Unfortunately, the chosen integration time of ∼15 min was not sufficient to detect the two sources at 70 μm, where the uncertainties in the SED were the highest. The PACS flux density of both targets was measured in an aperture of 10 arcsec radius, corrected for the encircled energy fraction (see the PACS Observers' Manual[2]) and are reported in Table 1. At 70 μm we only report the 1σ upper limits.

2.3 Radio observations

SDP.81 was observed by the Extended Very Large Array (EVLA) for two 3 h tracks during 2010 July 17–18 (programme AI143/10A-253), when the EVLA was in its most compact configuration (D), recording data every 1 s and using 16 Ka-band antennas. Antenna pointing was checked at 5 GHz. Much of the first track suffered from a correlator problem and was discarded. For SDP.81, the ^{12}CO $J = 1-0$ line [hereafter CO(1–0)] is redshifted to 28.53 GHz for $z = 3.042$, a frequency at which just one of the two sub-band pairs of the EVLA's new Ka-band receivers could be utilized, yielding 128 MHz of instantaneous, dual-polarization bandwidth during the earliest shared-risk phase of EVLA commissioning with the new Wide band Interferometric Digital Architecture correlator. For our observations at 8.40 GHz, we obtained 256 MHz of contiguous, dual-polarization bandwidth. In total, we recorded 2 h of data at 8.40 GHz and a similar amount at 28.53 GHz, resulting in an overall on-source integration time of ∼85 min. 3C 286 was used for absolute flux calibration, and the local calibrator, J0909+0121, was observed every 5 min.

Editing and calibration were accomplished within AIPS (31DEC10). For 3C 286, we used an appropriately scaled 22.5 GHz model to determine gain solutions; J0909+0121 was used to determine the spectral variation of the gain solutions (the 'bandpass'), after first removing atmospheric phase drifts on a time-scale of 12 s via self-calibration with a simple point-source model. We were able to employ standard AIPS recipes throughout the data-reduction process, following the techniques employed by Ivison et al. (2010b). The

[2] The PACS Observers' Manual is available from the Herschel Science Centre: http://herschel.esac.esa.int/Docs/PACS/pdf/pacs_om.pdf.

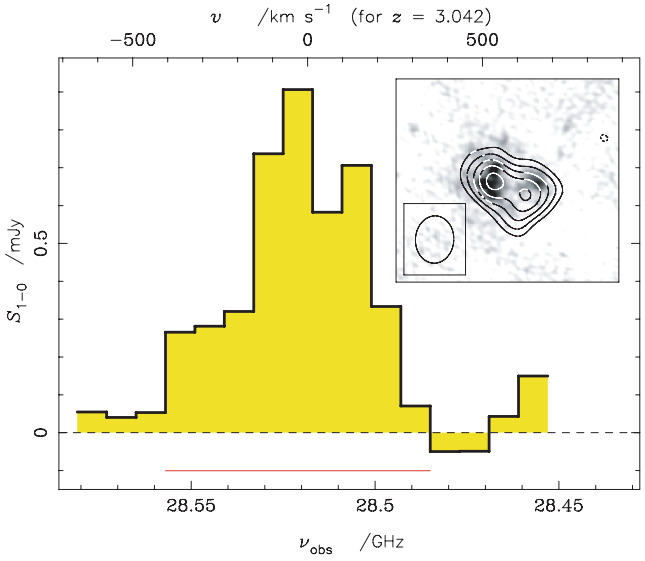


Figure 1. Spectrum of ^{12}CO $J = 1$–0 line emission from SDP.81 from the Expanded Very Large Array. *Inset:* Contours of the CO(1–0) emission, integrated across the velocity range −400 to +350 km s^{-1} (indicated by the line below the spectrum, and where $v = 0$ km s^{-1} at 28.51836 GHz for $z = 3.042$), which corresponds roughly to the FWZI of the line, overlaid upon a grey-scale SMA 880 μm continuum image (scaled from 0–8 mJy) presented by Negrello et al. (2010). The synthesized beam for the CO observations is shown in the inset, bottom left (3.3 × 2.4 arcsec^2), and the contours are plotted at −2.5, 2.5,3.5... 6.5× σ, where the rms noise level, $\sigma = 100$ μJy beam^{-1}. The synthesized beam for the continuum observations is ≈12 × 8 arcsec^2 and the size of the image is 20 × 20. arcsec^2.

synthesized beam for the CO observations is 3.3 × 2.4 arcsec^2 and ≈12 × 8 arcsec^2 for the continuum.

Fig. 1 summarizes the result of the EVLA observations for SDP.81. For CO(1–0), we measure an integrated line flux of 1.26 ± 0.20 Jy km s^{-1}, consistent with the GBT value of 1.11 ± 0.25 Jy km s^{-1} (Frayer et al. 2011), the full width at zero intensity (FWZI) is ∼750 km s^{-1}. At 8.40 GHz, we measure a total flux density of $S_{8.4\,\mathrm{GHz}} = 700 \pm 50$ μJy. A contour plot of the integrated CO(1–0) emission is shown in the inset of Fig. 1, overlaid on a grey-scale 880 μm continuum emission from the Submillimeter Array (SMA).

SDP.81 was observed and detected with the Institut de Radioastronomie Millimétrique (IRAM) Plateau de Bure Interferometer (PdBI) at 240 GHz and at a resolution of 0.62 × 0.30 arcsec^2 on 2010 February 15 (Neri et al. in preparation). SDP.81 was also observed at higher resolution with the Combined Array for Research in Millimeter-wave Astronomy (CARMA) on 2010 February 22 and 23 (program cx306), when CARMA was in its most extended A configuration at 240 GHz. Due to previously arranged scheduling plans, the phase monitoring array was not deployed during these observations. However, the phase rms was less than 100 μm, and the atmospheric opacity at 230 GHz (or $\tau_{230\,\mathrm{GHz}}$) was less than 0.2 at zenith, allowing the observations to go ahead without the monitoring array. The full width at half-maximum (FWHM) size of the test calibrator was 0.19 × 0.14 arcsec^2, while the theoretical beam size is 0.17 × 0.14 arcsec^2. This is pretty good agreement and suggests that atmospheric 'seeing' was not a big problem during the observations.

The CARMA observations of SDP.81 were in two ∼5 h tracks, the noise obtained from the first track being much higher than the second, due to the higher atmospheric opacity. Therefore, the two

Downloaded from https://academic.oup.com/mnras/article-abstract/415/4/3473/1748743
by Imperial College London Library user
on 11 December 2017

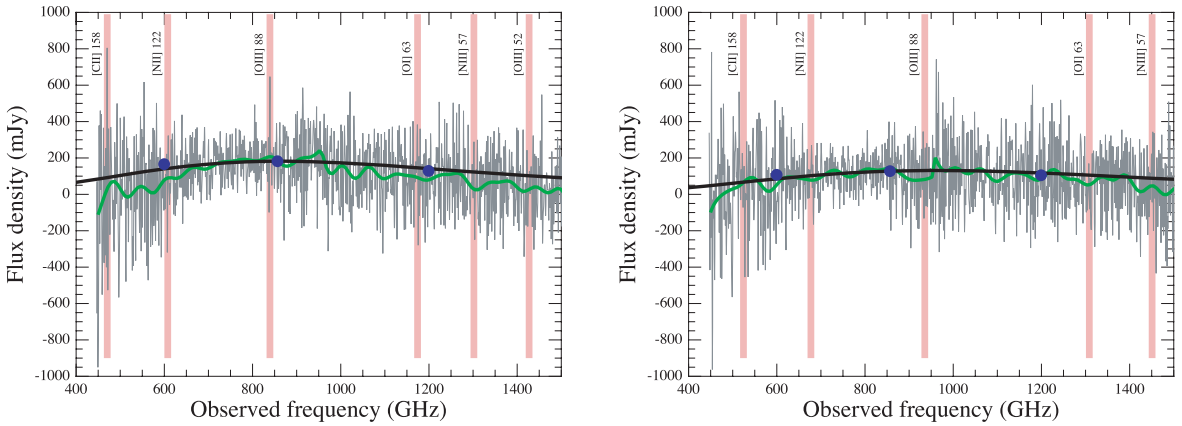


Figure 2. The FTS high- and low-resolution spectra of SDP.81 (left-hand panel) and SDP.130 (right-hand panel) overlaid with the three SPIRE photometric points (dots) and the SED template fit. The photometric errors, even including the 7 per cent flux calibration uncertainty of the SPIRE Photometer, are smaller than the dots. The expected positions of a number of fine-structure lines are indicated with vertical bars.

tracks were not co-added, and only the results from second track that was observed in $\tau_{230\,\mathrm{GHz}} = 0.1$ are presented here. The data were reduced with and without a Gaussian taper of 0.3 arcsec. The taper reduces the resolution (and sensitivity), but may pick out low-level emission. SDP.81 was not detected in either case, and the 240 GHz respective resolutions and sensitivities reached with CARMA were 0.17×0.14 arcsec^2 and 0.67 mJy beam^{-1} in the no-taper and 0.30×0.26 arcsec^2 and 1.1 mJy beam^{-1} in the 0.3 arcsec-taper maps.

SDP.81 is also present in the FIRST survey (Becker, White & Helfand 1995) at 1.4 GHz with $S_{1.4\mathrm{GHz}} = 950 \pm 150$ μm.

3 SPIRE FTS DATA PROCESSING

In this section we briefly describe our data-processing approach and underline where it deviates from the standard SPIRE FTS data processing. Detailed description of the standard FTS pipeline can be consulted in the SPIRE Data Reduction Guide.[3]

Each of the three observations, two targets and one reference dark/off-target, are processed separately out to the final spectrum. The forward and the reverse scans are kept separated throughout the whole processing. We consider only the central detectors of the two SPIRE FTS short-wavelength (SSW) and long-wavelength (SLW) bolometer arrays. Note that the off-axis bolometers are of a limited use as the optical path and the standing-wave (fringe) pattern in the interferograms are very different. The fringes are at high optical path differences and consequently they have the undesirable effect of adding a fixed pattern noise that affects the high-resolution part of the spectrum.

The FTS detector timelines, sampled at 80 Hz, are first cleaned of glitches due to high-energy particles hitting the substrate, the bolometers or the readout electronics. The glitch removal utilizes a wavelet-based method. The fraction of samples identified as glitches was ∼0.5 per cent for the SSW and ∼0.8 per cent for the SLW for the three observations. Next, instrumental effects are removed: electrical cross-talk and time-domain phase correction. Then we convert the bolometer-recorded voltage into its temperature using a calibration between the bolometer resistance and temperature, established during ground testing. This is in contrast to the standard voltage-based pipeline FTS processing, where a non-linearity correction is applied to the read-out voltages. The reason for using the bolometer's net temperature is that it represents much more closely the physical response of the bolometer to incident radiation and therefore 'naturally' accounts for any non-linearity and drift in that response. In the circumstances we are faced with here, where we are critically dependent on being able to accurately subtract two large signals to give a very small one, we have found that this, combined with the interactive phase correction steps, gives a small but significant improvement over the current pipeline processing. It may be that using the temperature-based pipeline ends up being unnecessary with further improvements in the voltage-based pipeline, but for the time being we prefer this method, to remove any dependency on the drift correction and non-linearity steps which could inject systematic uncertainties into the data.

The resulting detector timelines are then converted to interferograms with the use of the spectrometer mirror mechanism timeline that provides the optical path difference (OPD) at each time sample. Thus, at the end of this step we have interferograms of signal versus OPD. The 100 forward and 100 reverse interferograms are then divided into 2^{18} parts, which we shift iteratively in the zero-path difference until the interferograms are precisely aligned, removing any residual phase shift introduced by the detectors' temporal response and beamsplitters (Naylor et al. 2010; Spencer et al. 2010). The interferograms from all 200 scans are then merged, the forward and the reverse ones separately; they are baseline corrected and during the averaging process the data points which are marked as glitches are discarded. The next steps include gain correction and phase correction of the interferograms, which are further zero padded and converted to the spectral domain using fast Fourier transforms. To convert the flux to physical units (Jy) and to correct for the relative spectral response function, we use a deep observation of Uranus. At this stage, the forward and reverse interferograms are averaged together. This procedure was followed for the two targets and the reference sky. The last step is the subtraction of the reference sky from the target, and the resulting spectra of SDP.81 and SDP.130 are shown in Fig. 2.

As we described in the previous section, the absolute continuum calibration, especially for faint targets, is quite difficult. Small changes, of the order of few tens of mK, in the temperature of the instrument and the telescope during the reference dark-sky observation and the target observations can lead to quite significant offsets in the continuum level. We iteratively adjusted the overall dark-sky level in order to get the best match with the available photometric points (Swinyard et al., in preparation). A further correction was

[3] Available at http://herschel.esac.esa.int.

Downloaded from https://academic.oup.com/mnras/article-abstract/415/4/3473/1748743
by Imperial College London Library user
on 11 December 2017

applied to the SLW spectra for both targets in order to remove the effect of variations in instrument temperature (Spencer et al. 2010). These corrections are already applied to the spectra shown in Fig. 2. Note that the continuum offset affects the low-resolution continuum too. This makes the use of the FTS in low-resolution mode, for an SED-like measurements, not very suitable, especially for faint targets.

4 RESULTS

The FTS covers the wavelength region from 197 to 670 μm. Some of the most prominent and well-studied ISM cooling lines fall in this range for the redshifts of the two targets in this study. The FTS spectral resolution is $\Delta\nu = 1.2$ GHz for the high-resolution mode and it is constant in frequency space. This spectral resolution corresponds to instrumental line FWHM from 280 to 970 km s^{-1} over the FTS spectral range. The measured FWHM of the CO(1–0) line is 440 ± 50 km s^{-1} (Frayer et al. 2011), also compatible with the EVLA measurement (see Fig. 1). This means that some lines could be marginally resolved at $\lambda < 300$ μm.

The instrumental line shape of all FTS instruments is a sinc function due to the truncation of the interferogram by the limited travel of the moving mirror. This function is characterized by one central peak and a number of secondary maxima at lower intensity. There are techniques to suppress the secondary maxima at the price of lowering the resolution, the so-called apodization (Naylor & Tahic 2007); however, we did not perform this additional smoothing as we are looking for very faint features. The SPIRE FTS instrumental line shape is very close to a sinc function, with noticeable asymmetry of the first high-frequency minimum. The reason for this asymmetry is still under investigation by the SPIRE instrument team. This may have very small effect on the line-flux measurements; however, the line centroids are not affected, as it was shown that the centroids of CO-ladder lines in nearby sources are as good as 1/20 of the resolution element (SPIRE OM 2010).

Thanks to the already available high-accuracy spectroscopic redshifts for the two galaxies (Lupu et al. 2010; Negrello et al. 2010; Frayer et al. 2011), we know where to search for lines at specific wavelengths. We fit a sinc function model to the continuum-subtracted spectrum in ±5000 km s^{-1} rest frame, around the expected positions of a number of ISM lines:

$$I(v) = I(0)\,\frac{\sin((v - v_0)/v_\sigma)}{(v - v_0)/v_\sigma}, \tag{1}$$

where v_σ is the sinc linewidth in km s^{-1}, measured between the two zero crossings nearest to the peak and v_0 is the line-centroid offset from the expected position for the given redshift. For the high-resolution mode, we have $v_\sigma = 1.193\ (\lambda_c/\mu\mathrm{m})$ km s^{-1}at the line centroid λ_c, we keep this parameter fixed. Note that the line FWHM is $v_{\mathrm{FWHM}} = v_\sigma/1.20671$. The output parameters are the line peak $I(0)$ and the line-centre offset v_0. The integrated line flux for a sinc function is then calculated using

$$S_{\mathrm{line}} = 0.012\,\left(\frac{I(0)}{\mathrm{mJy}}\right) \times 10^{-18}\,\mathrm{W\,m^{-2}}, \tag{2}$$

and the line luminosities with

$$L_{\mathrm{line}} = 3.11 \times 10^7\,\left(\frac{S_{\mathrm{line}}}{10^{-18}\,\mathrm{W\,m^{-2}}}\right)\,\left(\frac{D_{\mathrm{L}}}{\mathrm{Gpc}}\right)^2\,L_\odot, \tag{3}$$

where D_{L} is the luminosity distance.

4.1 SDP.81

The most prominent features in the FTS spectrum of SDP.81 are the [O III] 88 μm and [C II] 158 μm lines, clearly seen in Fig. 2, left-hand panel. The continuum-subtracted spectral segments of SDP.81, at ±5000 km s^{-1} rest frame around both lines, are shown in Fig. 3. The derived emission-line parameters from the sinc model fit are given in Table 2.

We detect the $^2P_{3/2}-^2P_{1/2}$ [C II] line at 158 μm, at an SNR of ∼5 (see Fig. 3, left-hand panel). The line falls near the longer wavelength end of the FTS spectrum, in a region in which the instrument contribution dominates even above the telescope background emission and consequently it is visibly noisier (see Fig. 2, left-hand panel). The other prominent feature is the $^3P_1-^3P_0$ [O III] 88 μm line, which is the third detection of this line at $z > 0.05$ (Ferkinhoff et al. 2010). We do not detect at a sufficient significance any of the other possible ISM lines that fall in the FTS range. For those lines we give the upper limits in Table 3.

4.2 SDP.130

We do not have any positive line detection in the FTS spectrum of SDP.130. Even stacking the spectra around all the lines in Tables 2

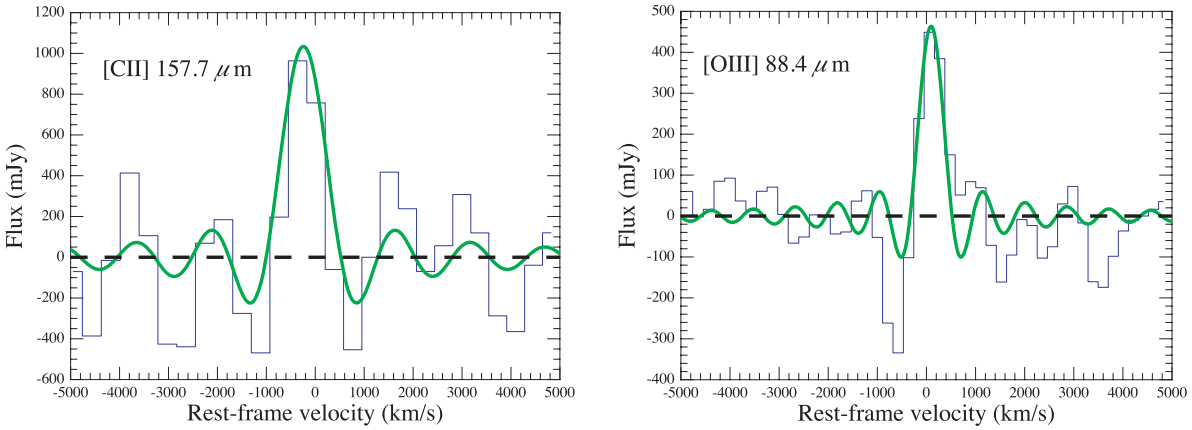


Figure 3. Continuum-subtracted regions within ±5000 km s^{-1} rest frame for [C II] 157.7 μm (left-hand panel) and [O III] 88.4 μm (right-hand panel) lines of SDP.81. The FTS data processed using two reference dark-sky observations (see Section 3) are shown as a histogram. The dashed line indicates the zero level. The best-fitting sinc function is also shown.

Downloaded from https://academic.oup.com/mnras/article-abstract/415/4/3473/1748743
by Imperial College London Library user
on 11 December 2017

Table 2. Characteristics of the [C II] and [O III] lines in SDP.81, as derived with a sinc function fit. We use $\mu_L\, L_{IR}(3\text{–}2000\ \mu m) = (5.13 \pm 0.88) \times 10^{13}\, L_\odot$ and $\mu_L = 25 \pm 7$, based on an improved lens model for SDP.81, which is different but still compatible with $\mu_L = 19$ quoted in Negrello et al. (2010). The reported velocity offset v_0, *in rest frame* km s^{-1}, is between the fitted line centroid and the expected one for the CO-measured redshift $z = 3.042$. The instrumental line FWHM in km s^{-1} corresponds to the high spectral resolution of 1.2 GHz; we keep this parameter fixed for the sinc fit. The noise rms is the standard deviation of the residual (fitted model subtracted from the data) in the velocity range ±5000 km s^{-1}. The reported SNR is the fitted line peak divided by the noise rms. The integrated line flux and line luminosity are calculated using equations (2) and (3), respectively. The errors are statistical errors; they do not include the FTS flux calibration uncertainty, conservatively estimated to be 15–20 per cent for wavelengths less than 300 μm and 20–30 per cent for wavelengths above 300 μm.

Characteristics	[O III] 88.4 μm	[C II] 157.7 μm
Fitted line centroid λ_c (μm)	357.2 ± 0.6 (839 GHz)	638.4 ± 1.8 (490 GHz)
Redshift	3.041 ± 0.006	3.046 ± 0.011
Velocity offset v_0 (km s^{-1})	95 ± 30	−240 ± 60
Instrumental line FWHM v_{FWHM} (km s^{-1})	514	919
Fitted line peak $I(0)$ (mJy)	480 ± 70	1100 ± 160
Noise rms (mJy)	90	211
SNR	5.4	5.2
Line flux S_{line} ($\times 10^{-18}$ W m^{-2})	5.8 ± 0.8	13.2 ± 1.9
Velocity integrated line flux $S_{line}\,\Delta v$ (Jy km s^{-1})	210 ± 30	840 ± 120
Line luminosity $\mu_L L_{line}$ ($\times 10^{10}\, L_\odot$)	13 ± 2	29 ± 4
L_{line}/L_{IR} ($\times 10^{-3}$)	2.4 ± 0.5	5.6 ± 1.3

Table 3. Upper limits (3σ) for some ISM lines for SDP.81 that fall in the FTS spectral range. The upper limits were calculated using equation (2), assuming $I(0)$ to be 3σ of the noise standard deviation within ±5000 km s^{-1} around the expected line centre.

Line ID	λ_0 (μm)	S_{line} (10^{-18} W m^{-2})	$\mu_L L_{line}$ ($10^{10} L_\odot$)	L_{line}/L_{IR} ($\times 10^{-3}$)
[O III]	52.0	<4	<9	<1.7
[N III]	57.0	<4	<10	<1.9
[O I]	63.2	<5	<11	<2.2
[N II]	122.1	<5	<11	<2.2
[O I]	145.5	<8	<19	<3.6

and 3 does not result in any positive signal. This target is about 30 per cent fainter than SDP.81 at 350 μm (see Table 1 and Fig. 2). Scaling from SDP.81 and assuming the same luminosity of the [C II] 158 μm line, we estimate the expected line flux for SDP.130 to be $\sim 4.5 \times 10^{-18}$ W m^{-2}, taking into account the magnification factor. This is ∼3 times fainter than the measured integrated line flux of SDP.81. Consequently, to detect this line at the same significance would require nine times longer integration time. On the other hand, the CO(1–0) line luminosity of SDP.130 is 50 per cent higher than that of SDP.81 (see Frayer et al. 2011), so scaling directly with the molecular gas mass, we would expect to see a marginal, ∼3–3.5σ, [C II] 158 μm feature. There could be different reasons for a suppressed [C II] (e.g. Luhman et al. 2003), but also the scaling of the [C II] with the molecular mass may not be straightforward and tentatively may indicate different conditions of the ISM in SDP.130.

Because of the non-detection we have used the observation of SDP.130 as a second dark-sky measurement, which helped to minimize further the noise in the SDP.81 spectrum (see Section 2.1).

4.3 Physical characteristics of the emitting region in SDP.81

We follow the analysis presented in Hailey-Dunsheath et al. (2010) and Stacey et al. (2010) using the PDR models of Kaufman et al. (1999) with the help of the PDR toolkit.[4] The expected physical conditions from the observed lines and the total infrared luminosity are given in terms of PDR cloud density n in cm^{-3} and the FUV ($6 < h\nu < 13.6$ eV) ionization field strength G_0, in units of the Habing field – the local Galactic interstellar radiation field of 1.6×10^{-3} erg cm^{-2} s^{-1}. We must emphasize that the results we derive are for a particular set of PDR models with pre-defined parameters, like the visual extinction of $A_V = 10$ and metallicity equal to the local ISM metallicity, i.e. $Z = Z_\odot$. At much lower metallicities, i.e. $Z = 0.1\, Z_\odot$ and smaller A_V we would expect that the derived n and G_0 will change by ∼10 per cent (Kaufman et al. 1999). In addition, as SDP.81 is unresolved, the derived PDR characteristics are an ensemble average of possibly many PDRs falling in the SPIRE-FTS beam. This has an implication for the comparison with the PDR models of Kaufman et al. (1999) using optically thick lines, like the CO transitions or the [O I] 63 μm line. The CO(1–0) emission in SMGs typically comes from a relatively smooth, optically thick medium (e.g. Carilli et al. 2010) with some substructure that may become more prominent in higher J lines and the continuum. For such a medium, CO observations could probe higher by a factor of 2 column densities. None the less, in the subsequent analysis, following Kaufman et al. (1999) and other works (e.g. Swinbank et al. 2010; Danielson et al. 2011), we double the observed luminosities of the optically thick lines in order to account for the fact that we see the emission only from one side of the clouds.

4.3.1 [C II] 158-μm line

The [C II] line at 158 μm is one of the best studied ISM collisionally excited lines. It is a widespread coolant for the ISM in galaxies; it requires only relatively modest FUV fluxes to be produced, and hence it traces star formation rather than active galactic nucleus (AGN) activity. This line can account for up to 1 per cent of the

[4] The PDR-modelling toolkit (Pound & Wolfire 2007) is available at http://dustem.astro.umd.edu.

Downloaded from https://academic.oup.com/mnras/article-abstract/415/4/3473/1748743
by Imperial College London Library user
on 11 December 2017

total FIR luminosity in normal galaxies (e.g. Stacey et al. 1991) and is optically thin in most cases. A large fraction of the [C II] luminosity comes from PDRs; however, a non-negligible fraction of the [C II] emission may arise from a diffuse ionized gas and from H II regions. The usual approach to estimate this fraction is with the [N II] 122 μm line (see e.g. Malhotra et al. 2001; Contursi et al. 2002; Oberst et al. 2006; Vasta et al. 2010). Nitrogen has the ionization potential of 14.53 eV, higher than 13.6 eV of hydrogen, and so the [N II] 122 μm line can only originate from H II regions or from the diffuse ionized medium. When there is not enough information from other lines, which is the case for most of the high-redshift SMGs, it is assumed that 70 per cent of the [C II] emission arises in the PDR (e.g. Hailey-Dunsheath et al. 2010; Stacey et al. 2010) based on Oberst et al. (2006) measurements in our Galaxy (the Great Carina nebula) and also supported by observations of nearby normal galaxies (Malhotra et al. 2001). We follow the same approach and adopt the same 70 per cent fraction of [C II] coming from a PDR, which is consistent with the observed lower limit of the [C II]/[N II] ratio of 2.6 in SDP.81, which, compared to the ratio of 1.6 from a pure H II region, means that at least 40 per cent of the [C II] flux comes from PDRs.

The ionizing UV source can be either hot stars or an AGN, and this increases the complexity when one wants to derive the physical conditions based on cooling lines in the FIR. A line ratio, involving [C II], that can be used to infer the origin of the radiation field, is $L_{[O\,I]63\mu}/L_{[C\,II]}$ (Meijerink, Spaans & Israel 2007; Abel et al. 2009). The upper limit of this ratio for SDP.81 is 1.1, which is characteristic for environments excited by stellar radiation, but also overlaps marginally with the allowed region for AGN excitation, which would require a line ratio greater than 1 (Abel et al. 2009). Thus, we have to keep in mind that part of the ionizing radiation field may have contribution from an AGN. The FIR lines are not a sensitive indicator of an AGN (see e.g. Graciá-Carpio et al. 2011) which makes it difficult to quantify this fraction. In the subsequent PDR analysis, we assume that the radiation field is due to UV coming from hot stars.

An idea of the physical conditions, in terms of the FUV radiation field strength G_0 and PDR density n, can be obtained by comparing the fractional [C II] luminosity versus the fractional CO(1–0) luminosity with PDR models (Stacey et al. 1991; Hailey-Dunsheath et al. 2010; Ivison et al. 2010d; Stacey et al. 2010). In the diagram shown in Fig. 4, where we have used the EVLA CO(1–0) measurements from this work, we can see that even with the [C II] alone SDP.81 is comprised of PDRs with a mean density of $\sim 10^2$–10^4 cm^{-3} and $G_0 \sim 10^2$–10^3, similar to other star-forming galaxies at $z = 1$–2 and to SMMJ2135 (Ivison et al. 2010d). We can compare the relative strength of the [C II] line, in terms of the FIR luminosity, with other galaxies with measured [C II] lines (see e.g. Maiolino et al. 2009; Stacey et al. 2010; Graciá-Carpio et al. 2011). SDP.81 has $\log(L_{[CII]}/L_{FIR}) = -2.2 \pm 0.05$ – one of the highest observed ratios, which contrasts with the deficiency reported for the ultra-luminous infrared galaxy (ULIRG) and AGN (e.g. Luhman et al. 2003). Although it might seem that SDP.81 relative [C II] strength is much higher than the one seen in AGNs at $z = 1$–2, recent measurements

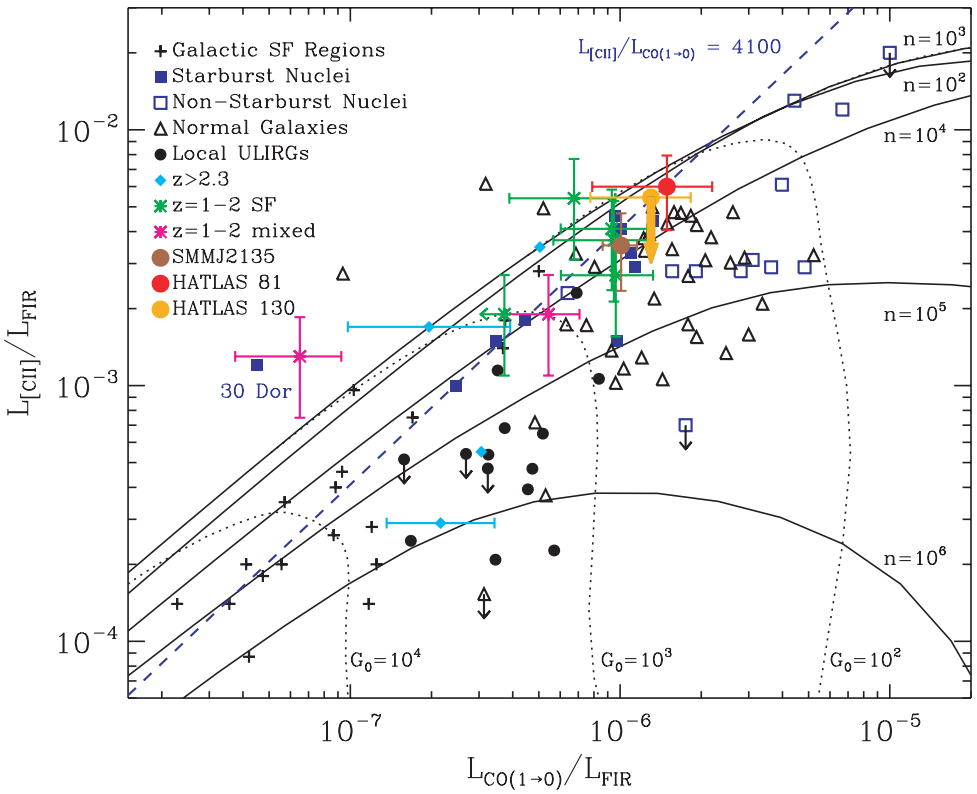


Figure 4. Diagnostic diagram of $L_{[CII]}/L_{FIR}$ as a function of $L_{CO(1-0)}/L_{FIR}$ for SDP.81 (the rightmost filled circle) and SDP.130 (filled circle with a down arrow), compared to local and other known high-redshift galaxies of different classes (Stacey et al. 1991, 2010; Hailey-Dunsheath et al. 2010). The lines with the constant density n and constant G_0 from PDR models of Kaufman et al. (1999) are also shown. The [C II] luminosity was corrected for the fraction of the flux arising from H II and diffuse ionized regions. The CO(1–0) line flux from the EVLA measurement was multiplied by 2 to take into account that the line is optically thick and we see only the fraction coming from the illuminated PDR side. $L_{[C\,II]}/L_{CO(1-0)}$ of 4100, typical for local starburst galaxies, is also shown as a dashed line. We have used $L_{FIR}(42.5\text{–}122.5\ \mu m) = L_{IR}(3\text{–}2000\ \mu m)/1.54$, derived by integrating the SED of SDP.81.

© 2011 The Authors, MNRAS **415,** 3473–3484
Monthly Notices of the Royal Astronomical Society © 2011 RAS

Downloaded from https://academic.oup.com/mnras/article-abstract/415/4/3473/1748743
by Imperial College London Library user
on 11 December 2017

with the *Herschel* PACS instrument, however, do not show any clear separation between local AGN systems [quasi-stellar object (QSO), Seyferts, low-ionization nuclear emission regions (LINERS)], starbursts and infrared luminous galaxies (Graciá-Carpio et al. 2011).

The ratio $L_{[\mathrm{C\,II}]}/L_{\mathrm{CO}(1-0)}$ of ∼4000 is quite close to the average of 4100 for normal metallicity star-forming galaxies or Galactic star formation or molecular clouds (Madden 2000; Stacey et al. 2010). It is also important to note that in comparison with the other high-redshift galaxies, SDP.81 has one of the highest fractional [C II] and CO(1–0) luminosities. Whether this is significant or it is simply due to luminosity bias is to be confirmed by increasing the number of high-redshift SMGs at $L_{\mathrm{FIR}} < 10^{12}\,\mathrm{L}_{\odot}$.

The diagram shown in Figs 4 is quite useful as diagnostic and as a comparison with other observations of galaxies of different classes. To properly quantify the physical conditions, we can add all the available information: the PDR luminosity of [C II], the total FIR luminosity, the upper limit of the [O I] 63 μm line and the EVLA detections of CO(1–0) and perform a least-squares fit with grids of PDR models with a different (n, G_0). Using the PDR toolkit (Pound & Wolfire 2007), we derive the best-fitting PDR density of $n = 10^{3.30\pm0.22}\,\mathrm{cm}^{-3}$, which is in very good agreement with the H_2 density from RADEX models using the CO lines (Lupu et al. 2010, model m03). The corresponding radiation field strength is $G_0 = 10^{2.24\pm0.19}$. The confidence χ^2 region in the (n, G_0) plane, delineated by the line ratios, is shown in Fig. 5. These (n, G_0) values correspond to a PDR surface temperature of $T_{\mathrm{s}} \approx 200\,\mathrm{K}$.

Adding the CO(7–6) line from Lupu et al. (2010), and considering only the two ratios [C II]/CO(1–0) and CO(7–6)/CO(1–0), we obtain an order-of-magnitude higher values: $n \approx 3.2 \times 10^4\,\mathrm{cm}^{-3}$ and $G_0 \approx 5.6 \times 10^3$, as shown in Fig. 5. This is to be expected as the CO(7–6) line usually traces higher density regions. In addition, it must be noted that CO(7–6) is likely to be blended with [C I] given the relatively coarse resolution of the Z-Spec spectrometer. Recent measurements with *Herschel* show that [C I] has approximately 50–150 per cent of the flux of the CO(7–6) line, 80 per cent on average, based on a sample of 20 local ULIRGs (van der Werf et al, in preparation). Even taking into account the blending, i.e. scaling down the CO(7–6) line flux by a factor of 1.8, the overall picture does not change significantly. It should be noted that G_0 derived from [C II] should be more representative for the PDR as a whole, since the [C II] line comes from PDRs *and* molecular cloud surfaces. Consequently, in the following analysis we use the low (n, G_0) values (i.e. not taking into account the CO(7–6) line).

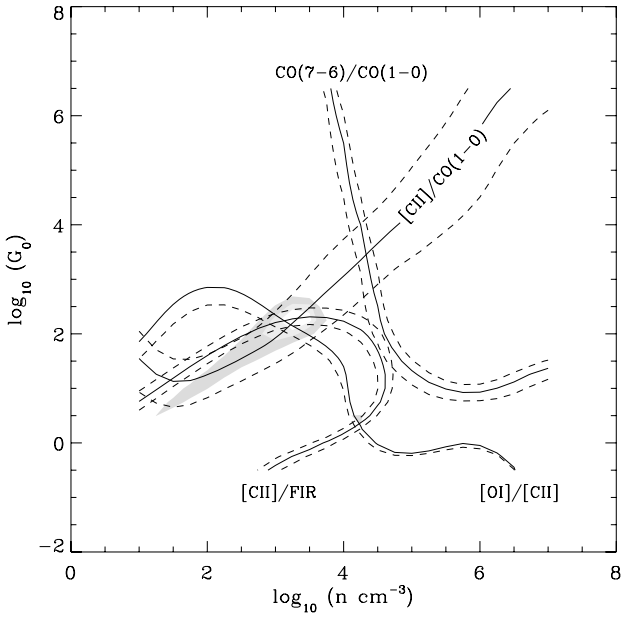


Figure 5. PDR model predictions for the density (n) and the FUV flux (G_0) from the observed line ratios. The [O I] 63 μm/[C II] 158 μm is shown as an upper limit, the dashed line indicating the side where we expect the ratio to be if [O I] is less luminous. The shaded contours show the 3σ confidence region of the expected (n, G_0) values when considering only [C II], CO(1–0) and the upper limit on [O I]. The CO(7–6)/CO(1–0) ratio was corrected for [C I] blending with CO(7–6).

A straightforward use of the PDR-derived characteristics is to investigate the effective physical size of the non-lensed-emitting region. With a PDR density, n, of ≈2000 cm^{-3} and the total gas mass from Lupu et al. (2010) of $M_{\mathrm{gas}} = 1.3 \times 10^{11}\,\mathrm{M}_{\odot}/\mu_{\mathrm{L}}$, where μ_{L} is the magnification factor of 25 ± 7, we obtain the effective radius of the PDR-emitting region of $\sim 1.0\,\mathrm{kpc}/\mu_{\mathrm{L}}^{1/3}$ or (0.3–0.4) kpc for a spherical distribution. For a disc geometry with a thickness of 100 pc, the radius is $\sim 3.0\,\mathrm{kpc}/\sqrt{\mu_{\mathrm{L}}}$ or (0.5–0.7) kpc correspondingly. This result is in good agreement with the equivalent dust-emitting radius of 0.7 kpc for SDP.81 derived in Lupu et al. (2010) and the size of the emitting region in SMMJ2135 (Danielson et al. 2011).

Although the SPIRE FTS' smallest beam size is 17 arcsec FWHM, nevertheless we can have an idea of the effective magnified size of the [C II]-emitting region by means of the [C II] beam filling factor. Assuming that the PDR slab is illuminated from one side by a flux G_0 and that dust grains are heated by the FUV photons then we can compare the model-predicted [C II] line intensity (Kaufman et al. 1999) with the observed line intensity and thus we can derive the beam-filling factor (Wolfire, Tielens & Hollenbach 1990) $\Phi_{\mathrm{A}} = (S_{[\mathrm{CII}]}/\Omega)/I_{[\mathrm{CII}]} \approx 3 \times 10^{-4}$, where $\Omega = 10^{-7}\,\mathrm{sr} = 1.22\,\mathrm{arcmin}^2$ is the SPIRE FTS effective beam area at the wavelength of the [C II] line (Swinyard et al. 2010). This corresponds to an effective radius of the magnified emitting region of ≈1 arcsec. This is consistent with the SMA-continuum observations and the EVLA CO(1–0) map, shown in Fig. 1.

We can also use the PDR results to place a lower limit on the H_2 mass of SDP.81, independently from the mass derived using CO measurements. Assuming that the [C II] line is optically, thin then the minimum total atomic hydrogen mass in the PDR (Crawford et al. 1985; Hailey-Dunsheath et al. 2010; Ivison et al. 2010d) is

$$M_{\mathrm{a}} = 0.77\,Q(T)\,\frac{L_{[\mathrm{C\,II}]}}{\mathrm{L}_{\odot}}\,\frac{1.4\times10^{-4}}{\chi(\mathrm{C}^+)}\,\mathrm{M}_{\odot}, \quad (4)$$

where $Q(T) = [1 + 2\mathrm{e}^{(-91\,K/T_s)} + n_{\mathrm{crit}}/n]/[2\mathrm{e}^{(-91\,K/T_s)}]$. Substituting the [C II] luminosity corrected for the H II contribution and for the magnification, the PDR surface temperature and density, the critical density of $\mathrm{C}^+\ ^2P_{2/3}$ level of $n_{\mathrm{crit}} = 2700\,\mathrm{cm}^{-3}$ (Launay & Roueff 1977) and the C^+ abundance $\chi(\mathrm{C}^+) = 1.4 \times 10^{-4}$ (Savage & Sembach 1996), we derive $M_{\mathrm{a}} \approx 1.7 \times 10^{10}\,\mathrm{M}_{\odot}$. It should be noted that this minimum atomic mass in the PDR is quite sensitive to the assumed PDR fraction of the [C II] luminosity, the magnification factor and the unknown real heavy element abundances. Nevertheless, the derived M_{a} is of the order of the estimated molecular gas mass $M(\mathrm{H}_2) = (1-3) \times 10^{10}\,\mathrm{M}_{\odot}$ derived from CO(1–0) (Frayer et al. 2011), somewhat higher than the fraction of 20–50 per cent seen in other high-redshift star-forming galaxies (Stacey et al. 2010).

Downloaded from https://academic.oup.com/mnras/article-abstract/415/4/3473/1748743
by Imperial College London Library user
on 11 December 2017

4.3.2 [O III] 88 μm line

The [O III] lines are usually connected with H II regions but also with AGN activity. The [O III] 88 μm line is emitted via the transition $^3P_1 - ^3P_0$ of O^{++}. The ionization potential of O^+ is 35 eV, which requires a nearby hot young star or stars ($T \sim 36\,000$–$40\,000$ K) or an AGN, to provide the necessary FUV photons. The [O III] line emission is quite sensitive to the effective temperature of the ionizing stars and if this temperature drops from 36 000 to 33 000 K the line intensity would drop by a factor of up to 30 (Rubin 1985). The ratio $L_{[\mathrm{O\,III}]}/L_{\mathrm{FIR}}$ observed in SDP.81 is significantly higher than the one observed in normal galaxies, although smaller than the ratio in irregular, H II-dominated galaxies (Malhotra et al. 2001; Graciá-Carpio et al. 2011). Comparing this ratio with models (Abel et al. 2009) indicates that some fraction of the emission may be due to an AGN source. The situation is not that clear, however, comparing $L_{[\mathrm{OIII}]}/L_{\mathrm{FIR}}$ with recent observations, which show no clear separation of the local AGN sources (Seyferts, QSOs, LINERs) and the rest (Graciá-Carpio et al. 2011). Thus, similar to the $L_{[\mathrm{OI}]\,63\mu}/L_{[\mathrm{C\,II}]}$ result, we cannot discard completely that some fraction of the ionizing field may arise in an AGN.

The detected [O III] 88 μm line can also provide us with information about the properties of an ensemble H II component, with [O III] emission coming from regions much closer to the UV sources (see e.g. Cormier et al. 2010; Okada et al. 2010). Transitions of the same ion O^{++} from different collisionally excited levels of the same fine-structure multiplet, as is the case for the two lines of [O III] at 52 and 88 μm, are not sensitive to the temperature, for a reasonably large range of the density, and can be used to estimate the electron density n_{e} in the H II region. Unfortunately, we do not detect [O III] at 52 μm; thus, we can only put an upper limit on $L_{[\mathrm{O\,III}]\,52\mu}/L_{[\mathrm{O\,III}]\,88\mu}$ of $\lesssim$0.7, which is quite close to the low-density limit of $n_{\mathrm{e}} \approx 100\,\mathrm{cm}^{-3}$ (see e.g. Rubin 1989; Fischer et al. 1999). This electron density is typical for galactic H II regions.

4.4 FIR/radio correlation and millimetre-imaging source constraints

In support for the hypothesis that some fraction of the ionizing radiation in SDP.81 may originate from an AGN is the radio data (see Section 2.3). In Fig. 6 we compare the SED of SDP.81 to the template used in Ivison et al. (2010d) for the SMMJ2135 (the cosmic 'Eyelash'), which follows the FIR/radio correlation. Combining $S_{8.4\,\mathrm{GHz}}$ with $S_{1.4\,\mathrm{GHz}} = 950 \pm 150$ μJy from the FIRST survey (Becker et al. 1995) yields a spectral index of $\alpha = -0.17^{+0.11}_{-0.09}$ (where $S_\nu \propto \nu^\alpha$), suggesting that an AGN is powering some fraction of the radio emission (Ibar et al. 2010a). Note however that a flat spectrum could also be a result from compact star-forming regions dominated by star formation (Hunt & Maiolino 2005). Combining the radio measurements with L_{IR} yields $q_{\mathrm{IR}} = 1.8 \pm 0.1$ (see Ivison et al. 2010c for details). This is only barely consistent with the FIR–radio correlation, providing more evidence that SDP.81 is moderately radio loud (cf. $q_{\mathrm{IR}} = 2.4$ for FIR-selected galaxies; see Ivison et al. 2010a,c, d; Jarvis et al. 2010; Michałowski, Hjorth & Watson 2010).

At millimetre band, the peak and the total 1 mm fluxes measured in a PdBI 0.62 × 0.30 arcsec^2 beam and ∼3 arcsec diameter area of SDP.81 are 2.4 and 7.5 mJy, respectively (Neri et al. in preparation), suggesting that the contribution of any strong compact (<0.54 arcsec) source, like an AGN, if it is indeed present in this object, would be at most 33 per cent of the total millimetre radiation. If the unresolved 20 mJy flux detected by the IRAM 30-m telescope at 2 mm is also considered (Negrello et al. 2010), then the PdBI-measured peak suggests the contribution of any strong compact source would be less than 14 per cent of the total flux at these wavelengths.

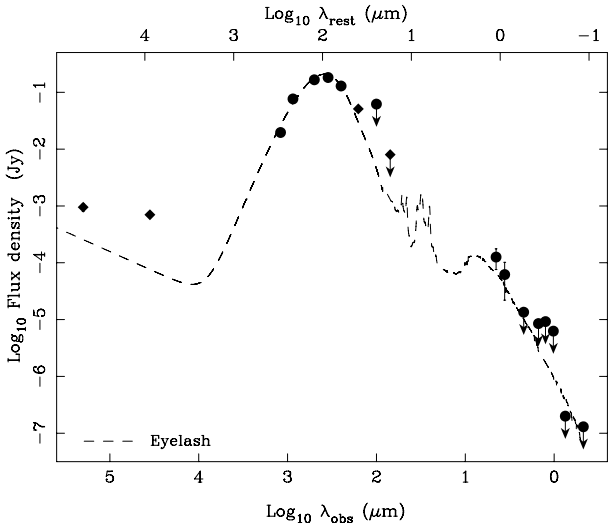


Figure 6. SED of SDP.81 including the new measurements presented in this paper: the radio observation at 8.5 GHz (see Section 2.3) and PACS 70 and 160 μm, all marked as diamonds. The 1.4 GHz detection of SDP.81 in the FIRST survey (Becker et al. 1995) is also shown. The dashed line is an Arp 220 template, as used for SMMJ2135 source (the cosmic 'Eyelash') reported in Ivison et al. (2010d) and that obeys the FIR/radio correlation. The filled circles represent data from Negrello et al. (2010) and Hopwood et al. (2011). The two radio measurements are clearly deviating from the FIR/radio correlation followed by other FIR-selected galaxies.

With higher resolution observations using CARMA in its most extended configuration, SDP.81 is not detected. The rms noise in the 0.17 × 0.14 arcsec^2 beam map is estimated at 0.67 mJy. Based on this and the peak emission in the PdBI observations, we conclude that if the peak emission in the PdBI image was a point source, it would have been detected; therefore, it has to be at least 0.15 arcsec to be consistent with the CARMA non-detection. This implies the 2.4 mJy peak emission measured in the PdBI beam cannot all come from a point source or AGN, putting an upper limit of the AGN flux contribution to no more than ∼1/3 (or 0.8 mJy) of the 2.4 mJy peak and ∼1/10 of the 7.5 mJy total millimetre emission detected by PdBI or ∼1/25 of the 20 mJy detected by the IRAM telescope. This is consistent with the continuum upper limit of 1 mJy measured at 1 cm in the EVLA observations, when extrapolated to the 1 mm wavelength regime for a radio-loud or flat-spectrum source.

Putting all the pieces together we can see that the physical conditions in SDP.81 are similar to other high-redshift star-forming galaxies, although SDP.81 is at somewhat lower intrinsic luminosity, but still being an ULIRG. The radio observations provide supporting evidence to the hints from the ISM lines that part of the ionization field in the galaxy may be due to an AGN. With the available observations we cannot put any strong constraint on this fraction, although a compact source contribution in the millimetre-band flux cannot exceed 33 per cent.

5 CONCLUSIONS

We have presented *Herschel*-SPIRE Fourier Transform Spectrometer (FTS) and radio follow-up observations of *Herschel*-ATLAS strongly lensed sources. Two targets, SDP.81 and SDP.130, were observed with the FTS, resulting in spectra over a wavelength range from 197 to 670 μm (447–1522 GHz) at a constant spectral

Downloaded from https://academic.oup.com/mnras/article-abstract/415/4/3473/1748743
by Imperial College London Library user
on 11 December 2017

resolution of 1.2 GHz. We also presented observations of SDP.81 with the EVLA, PdBI and CARMA in the radio domain, helping to better characterize the source properties.

Thanks to the lensing effect, boosting the luminosity of SDP.81 by a factor of ∼25, we were able to detect [C II] at 158 μm and [O III] 88 μm lines in its FTS spectra. We do not detect any plausible lines in the spectrum of SDP.130. We should have been able to marginally detect the [C II] 158 μm line at 3–3.5σ if we scale the [C II] with the molecular mass derived from ground-based CO(1–0) line measurements. If we assume the same ratio of [C II] to $L_{\rm IR}$ as in SDP.81, however, we do not expect detection – the line would be too faint. This is an indication of a possible difference in the quantity and the distribution of the molecular material in the two FTS targets, although the uncertainties are too important for any strong claim.

The successful line detections in SDP.81 allowed for detailed studies of the physical conditions in the emitting regions at $z \sim 3$. The clear and unambiguous detections of [O III] 88 μm and [C II] 158 μm allow us to measure the redshift using both lines. The derived value of $z = 3.043 \pm 0.012$, using the two lines, confirms the measured redshift of $z = 3.042$ from ground-based CO measurements. The detection of the [O III] 88 μm line is the third at redshifts higher than 0.05. We expect that the ongoing SPIRE and PACS spectroscopy with *Herschel* will lead to many more such line detections.

Combining the FTS-detected [C II] 158 μm line, the total infrared luminosity, the upper limit on the [O I] 63 μm line, the ground-based detections of the CO(1–0) transition we were able to infer a PDR cloud-ensemble density $n_0 \approx 2000\,{\rm cm}^{-3}$ and the FUV ionizing field strength $G_0 \approx 200$ in SDP.81. The PDR surface temperature is about 200 K, and the effective radius of the PDR-emitting region is of the order of 500–700 pc for a disc of 100 pc thickness. These characteristics are similar to other high-redshift star-forming galaxies.

The presence of a strong [O III] line, the upper limit of $L_{[{\rm O\,I}]63\mu}/L_{[{\rm C\,II}]}$ and the significant deviation from the FIR/radio correlation are all plausible indications that some fraction of the emission from SDP.81 may be due to an AGN source. The conservative upper limit of this contribution in the radio domain is estimated at ∼33 per cent.

The analysis presented in this paper is a clear illustration of the necessity of a combined effort from follow-up observations at different wavelengths in order to have a better idea of the physical conditions in the star-forming galaxies in the distant Universe. *Herschel* will be indispensable in this task, providing large samples of such galaxies for follow-up studies.

ACKNOWLEDGMENTS

We are indebted to S. Hailey-Dunsheath for making available his script and the data used to produce some of the figures, as well as for his valuable help with some of the interpretations. We thank Magda Vasta and Serena Viti for useful discussions.

The *Herschel*-ATLAS is a project with *Herschel*, which is an ESA space observatory with science instruments provided by European-led Principal Investigator consortia and with important participation from NASA. The H-ATLAS website is http://www.h-atlas.org/. PACS has been developed by a consortium of institutes led by MPE (Germany) and including UVIE (Austria); KU Leuven, CSL, IMEC (Belgium); CEA, LAM (France); MPIA (Germany); INAF-IFSI/OAA/OAP/OAT, LENS, SISSA (Italy); IAC (Spain). This development has been supported by the funding agencies BMVIT (Austria), ESA-PRODEX (Belgium), CEA/CNES (France), DLR (Germany), ASI/INAF (Italy), and CICYT/MCYT (Spain). SPIRE has been developed by a consortium of institutes led by Cardiff University (UK) and including Univ. Lethbridge (Canada); NAOC (China); CEA, LAM (France); IFSI, University of Padua (Italy); IAC (Spain); Stockholm Observatory (Sweden); Imperial College London, RAL, UCL-MSSL, UKATC, Univ. Sussex (UK); and Caltech, JPL, NHSC, Univ. Colorado (USA). This development has been supported by national funding agencies: CSA (Canada); NAOC (China); CEA, CNES, CNRS (France); ASI (Italy); MCINN (Spain); SNSB (Sweden); STFC (UK); and NASA (USA).

REFERENCES

Abel N. P., Dudley C., Fischer J., Satyapal S., van Hoof P. A. M., 2009, ApJ, 701, 1147
Baugh C. M., Lacey C. G., Frenk C. S., Granato G. L., Silva L., Bressan A., Benson A.J., Cole S., 2005, MNRAS, 356, 1191
Becker R., White R., Helfand D., 1995, ApJ, 450, 559
Blain A., 1996, MNRAS, 283, 1340
Brauher J. R., Dale D. A., Helou G., 2008, ApJS, 178, 280
Carilli C. et al., 2010, ApJ, 714, 1407
Contursi A. et al., 2002, AJ, 124, 751
Cormier D. et al., 2010, A&A, 518, L57
Crawford M. K., Genzel R., Townes C. H., Watson D. M., 1985, ApJ, 291, 755
Daddi E. et al., 2009a, ApJ, 694, 1517
Daddi E., Dannerbauer H., Krips M., Walter F., Dickinson M., Elbaz D., Morrison G. E., 2009b, ApJ, 695, L176
Danielson A. L. R. et al., 2011, MNRAS, 410, 1687
De Zotti G., Ricci R., Mesa D., Silva L., Mazzotta, P., Toffolatti L., González-Nuevo J., 2005, A&A, 431, 893
Devlin M. et al., 2009, Nat, 458, 737
Eales S. et al., 2010, PASP, 122, 499
Ferkinhoff C., Hailey-Dunsheath S., Nikola T., Parshley S. C., Stacey G. J., Benford D. J., Staguhn J. G., 2010, ApJ, 714, L147
Fischer J. et al., 1999, Ap&SS, 266, 91
Frayer D. et al., 2011, ApJ, 726, 22
Graciá-Carpio J. et al., 2011, ApJ, 728, L7
Greve T. R. et al., 2005, MNRAS, 359, 1165
Griffin M. et al., 2010, A&A, 518, L3
Hailey-Dunsheath S. et al., 2010, ApJ, 714, 162
Hollenbach D. J., Tielens A. G. G. M., 1997, ARA&A, 35, 179
Hopwood R. et al., 2011, ApJ, 728, 4
Hunt L. K., Maiolino R., 2005, ApJ, 626, L15
Ibar E., Ivison R. J., Best P. N., Coppin K., Pope A., Smail I., Dunlop J. S., 2010a, MNRAS, 401, 53
Ibar E. et al., 2010b, MNRAS, 409, 38
Ivison R. et al., 2010a, MNRAS, 402, 245
Ivison R. J., Smail I., Papadopoulos P. P., Wold I., Richard J., Swinbank A. M., Kneib J.-P., Owen F. N., 2010b, MNRAS, 404, 198
Ivison R. et al., 2010c, A&A, 518, L31
Ivison R. et al., 2010d, A&A, 518, L35
Jarvis M. et al., 2010, MNRAS, 409, 92
Kaufman M. J., Wolfire M. G., Hollenbach D. J., Luhman M. L., 1999, ApJ, 527, 795
Kramer C., Jakob H., Mookerjea B., Schneider N., Brüll M., Stutzki J., 2004, A&A, 424, 887
Lahav O., Liddle A., 2006, J. Phys. G: Nucl. Part. Phys. 21, 5
Launay J., Roueff E., 1977, J. Phys. B: At. Mol. Phys., 10, 879
Lilly S. et al., 1999, ApJ, 518, 641
Luhman M. L., Satyapal S., Fischer J., Wolfire M. G., Sturm E., Dudley C. C., Lutz D., Genzel R., 2003, ApJ, 594, 758
Lupu R. et al., 2010, ApJ, submitted (arXiv:1009.5983)
Madden S., 2000, New Astron. Rev., 44, 249
Maiolino R. et al., 2005, A&A, 440, L51
Maiolino R., Caselli P., Nagao T., Walmsley M., De Breuck C., Meneghetti M., 2009, A&A, 500, L1

Downloaded from https://academic.oup.com/mnras/article-abstract/415/4/3473/1748743
by Imperial College London Library user
on 11 December 2017

Malhotra S. et al., 2001, ApJ, 561, 766
Meijerink R., Spaans M., Israel F. P., 2007, A&A, 461, 793
Michałowski M., Hjorth J., Watson D., 2010, A&A, 514, 67
Naylor D., Tahic K., 2007, J. Opt. Soc. Am. A, 24, 3644
Naylor D. et al., 2010, in Oschmann J. M. Jr., Clampin M. C., MacEwen H. A., eds, SPIE Proc. Vol. 7731, Space Telescopes and Instrumentation 2010: Optical, Infrared and Millimeter Wave. SPIE, Bellingham, 773116
Negrello M., Perrotta F., González-Nuevo J., Silva L., de Zotti G., Granato G. L., Baccigalupi C., Danese L., 2007, MNRAS, 377, 1557
Negrello M. et al., 2010, Sci, 330, 800
Oberst T. E. et al., 2006, ApJ, 652, L125
Okada Y. et al., 2010, A&A, 514, A13
Ott S. et al., 2010, in Mizumoto Y., Morita K. I., Ohishi M., eds, ASP Conf. Ser. Vol. 434, Astronomical Data Analysis Software and Systems. Astron. Soc. Pac., San Francisco, p. 139
Pascale E. et al., 2011, MNRAS, in press, doi:10.1111/j.1365-2966.2011.18756.x (arXiv:1010.5782)
Pilbratt G. et al., 2010, A&A, 518, L1
Poglitsch A. et al., 2010, A&A, 518, L2
Pound M. W., Wolfire M. G., 2007, in Argyle R. W., Bunclark P. S., Lewis J. R., eds, ASP Conf. Ser. Vol. 394, Astronomical Data Analysis Software and Systems. Astron. Soc. Pac., San Francisco, p. 654
Riechers D. et al., 2010, ApJ, 720, L131
Rigby E. et al., 2011, MNRAS, submitted (arXiv:1010.5787)
Rubin R. H., 1985, ApJS, 57, 349
Rubin R. H., 1989, ApJS, 69, 897
Savage B. D., Sembach K. R., 1996, ARA&A, 34, 279
Smail I., Ivison R., Blain A., 1997, ApJ, 490, L5
Smith D. J. B. et al., 2011, MNRAS, submitted (arXiv:1007.5260)
Spencer L. D. et al., 2010, Meas. Sci. Technol., 21, 065601
SPIRE Observers' Manual, 2010, v2.2, *Herschel* Science Centre, HERSCHEL-DOC-0798
Stacey G. J., Geis N., Genzel R., Lugten J. B., Poglitsch A., Sternberg A., Townes C. H., 1991, ApJ, 373, 423
Stacey G. J., Hailey-Dunsheath S., Ferkinhoff C., Nikola T., Parshley S. C., Benford D. J., Staguhn J. G., Fiolet N., 2010, ApJ, 724, 957
Swinbank A. M., Chapman S. C., Smail I., Lindner C., Borys C., Blain A. W., Ivison R. J., Lewis G. F., 2006, MNRAS, 371, 465
Swinbank A. M. et al., 2010, Nat, 464, 733
Swinyard B. et al., 2010, A&A, 518, L4
Tacconi L. J. et al., 2006, ApJ, 640, 228
Tacconi L. J. et al., 2008, ApJ, 680, 246
Vasta M., Barlow M. J., Viti S., Yates J. A., Bell T. A., 2010, MNRAS, 404, 1910
Wagg J., Carilli C. L., Wilner D. J., Cox P., De Breuck C., Menten K., Riechers D.A., Walter F., 2010, A&A, 519, L1
Walter F., Riechers D., Cox P., Neri R., Carilli C., Bertoldi F., Weiss A., Maiolino R., 2009a, Nat, 457, 699
Walter F., Weiss A., Riechers D., Carilli C., Bertoldi F., Cox P., Menten K., 2009b, ApJ, 691, L1
Wolfire M. G., Tielens A. G. G. M., Hollenbach D., 1990, ApJ, 358, 116

This paper has been typeset from a TEX/LATEX file prepared by the author.

Downloaded from https://academic.oup.com/mnras/article-abstract/415/4/3473/1748743
by Imperial College London Library user
on 11 December 2017